Particle Accelerators, 1992, Vol. 39, pp.107–123
Reprints available directly from the publisher
Photocopying permitted by license only

PARAMETRIC BEAM INSTABILITY IN ALTERNATING-GRADIENT FOCUSING SYSTEMS

T. P. HUGHES

Mission Research Corporation, Albuquerque, NM 87106

D. CHERNIN

Science Applications International Corporation, McLean, VA 22102

A parametric electromagnetic instability is predicted for beam transport in arbitrary smooth-walled quadrupole focusing channels. The instability involves a resonant interaction between transverse sideband beam oscillations, produced by spatial harmonics of the quadrupole field, and transverse-electric modes of the drift tube. The instability does not occur in smooth focusing systems. A dispersion relation is derived and found to agree well with results of numerical simulations. Growth rates are potentially large for high-current, low-energy electron beam transport. Estimates for high-energy electron storage-ring and heavy-ion transport systems indicate that the instability is unlikely to be a problem in present designs of these devices.

1 INTRODUCTION

Alternating-gradient (AG) or 'strong' focusing[1] is widely applied in particle beam accelerators and storage rings. Usually, this type of focusing is implemented using a lattice of discrete magnetic quadrupoles whose poles are rotated by 90° from one quadrupole to the next. It is well known that as one increases the quadrupole strength, one encounters 'stop bands', or ranges of the quadrupole field gradient in which the single-particle orbits are unstable.[1,2] In addition, space-charge-induced instabilities have been predicted to occur for sufficiently strong field gradients.[3,4] In this paper, we show that beams in quadrupole channels are susceptible to a parametric instability involving a resonant interaction between the centroid motion and a transverse-electric (*TE*) mode of the beam pipe. This type of instability was previously encountered[5–7] in an analysis of the 'stellatron' accelerator,[8] which uses a continuous, rotating quadrupole field. Unlike the single-particle and space-charge instabilities mentioned, there is no threshold in quadrupole gradient or beam current; for a cold beam, the instability growth rate increases monotonically from zero with each of these quantities. There is, on the other hand, a resonance condition that must be satisfied. The interaction mechanism has some similarity to that in parametric electron beam amplifiers such as the 'Adler Tube.'[9]

The instability considered here is unlike the beam breakup and related instabilities involving cavities. For the latter, instability occurs because of the existence of 'slow'

electromagnetic waves ($v_{\text{phase}} < c$) with which the beam can resonate. In the present case, the parametric coupling of beam modes through the periodic focusing magnetic field allows these modes to interact with the fast electromagnetic waves of a smooth pipe.

In Section 2, we give two forms of the dispersion relation for the parametric instability. The first, based on Floquet's theorem, is exact but tends to obscure the nature of the interaction. A second, approximate polynomial form of the dispersion relation results in a simple interpretation in terms of intersecting modes in the ω-k plane. In Section 3, the predicted growth rates from the polynomial dispersion relation are compared favourably to the results from a numerical beam-centroid simulation of a low-energy, high-current beam. In Section 4, we consider two additional examples and find that the instability is unlikely to be seen in present high-energy electron storage rings or heavy-ion beam transport schemes.

2 DISPERSION RELATION

We consider a thin, monoenergetic electron beam propagating near the axis of a smooth wall cylindrical pipe. The beam is subject to external magnetic focusing by an arbitrary periodic quadrupole array of period L. We proceed to consider the interaction of such a beam with a TE_{1n} mode of the pipe, where n is the radial mode number. The centroid position of the beam, η, is a function of z (the axial coordinate) and time; it satisfies the equation

$$\ddot{\eta}(z,t) + \Omega^2(z)\eta(z,t) = \frac{e}{m\gamma c}\dot{a}(z,t) \quad , \tag{1}$$

where $\Omega^2(z+L) = \Omega^2(z)$ represents external focusing; a is the vector potential representing the amplitude of the TE_{1n} mode; and γ is the usual relativistic factor, $(1-v_z^2/c^2)^{-1/2}$, where v_z is the beam velocity in the axial direction and is assumed to be constant. In Eq. (1) a dot ($\dot{}$) represents $\partial/\partial t + v_z \partial/\partial z$.

The function $a(z,t)$ satisfies the wave equation

$$\left(\frac{\partial^2}{\partial z^2} - \frac{1}{c^2}\frac{\partial^2}{\partial t^2} - k_\perp^2\right) a(z,t) = \frac{-2\pi k_\perp^2}{I_{1n} c}\lambda(z,t)\dot{\eta}(z,t) \quad , \tag{2}$$

where $k_\perp = j'_{1n}/b$, $J_1'(j'_{1n}) = 0$, b is the pipe radius, J_1 is the Bessel function of the first kind, $I_{1n} = \pi(j_{1n}'^2 - 1)J_1^2(j'_{1n})$ and $\lambda(z,t)$ is the charge per unit length of the beam. See Appendix A for the derivation of this result.

If we take $\lambda(z,t)$ to be constant (i.e., an infinite, uniform beam), and take a Fourier transform in time ($\partial/\partial t \longrightarrow -i\omega$) of Eqs. (1) and (2), the resulting equations may be expressed as

$$\psi'(z) = T(z)\psi(z) \quad , \tag{3}$$

where $\psi(z)$ is the 4-element column vector

$$\psi(z) = \begin{pmatrix} \eta_\omega(z) \\ \eta'_\omega(z) \\ a_\omega(z) \\ a'_\omega(z) \end{pmatrix} \tag{4}$$

and $T(z) = T(z+L)$ is a 4×4 matrix

$$T(z) = \begin{pmatrix} 0 & 1 & 0 & 0 \\ \dfrac{\omega^2 - \Omega^2}{v_z^2} & \dfrac{2i\omega}{v_z} & \dfrac{-ie\omega}{m\gamma v_z^2 c} & \dfrac{e}{m\gamma v_z c} \\ 0 & 0 & 0 & 1 \\ \dfrac{2\pi k_\perp^2 \lambda i\omega}{I_{1n} c} & \dfrac{-2\pi k_\perp^2 \lambda v_z}{I_{1n} c} & k_\perp^2 - \dfrac{\omega^2}{c^2} & 0 \end{pmatrix} . \tag{5}$$

A prime, in Eqs. (3) and (4), denotes d/dz.

The four Floquet solutions to Eq. (3) satisfy

$$\psi^{(\ell)}(z+L) = e^{i\mu_\ell L}\psi^{(\ell)}(z) \tag{6}$$

for $\ell = 1, 2, 3, 4$, where the phase shift per period, $\mu_\ell L$, may be complex. These phase shifts are found by constructing the 4×4 matrix $\Psi(z)$, each column of which satisfies Eq. (3), and which satisfies the initial condition $\Psi(0) = I$ (the identity matrix). The phase factors $e^{i\mu_\ell L}$, $\ell = 1, 2, 3, 4$ are then the eigenvalues of $\Psi(L)$.

At this stage, of course, there is no reason to expect an instability; the analysis has been purely formal. If an instability does exist, the spatial growth rate is obtained by computing the eigenvalues of $\Psi(L)$, but even for the simplest lattice this is difficult to do analytically and numerical methods must be used.

We have carried out such a numerical procedure for the low-energy, high-current electron beam parameters in Table 1. The beam is coasting in a simple FD channel. Figure 1 shows a plot of the spatial growth rate, $Im(\mu_\ell)$, as a function of real frequency. Values indicated by a '+' were obtained by numerically computing $\Psi(L)$ and its eigenvalues; the solid lines were obtained from the approximate polynomial dispersion relation derived below. As is well known, a nonzero spatial growth rate does not necessarily indicate an instability. A method for distinguishing evanescent modes from unstable modes is given by Briggs[10] and involves examining the behavior of $Im(\mu_\ell)$ as a function of the imaginary part of ω. In principle, this method could be used here. In Fig. 1, however, we have identified 'unstable' and 'evanescent' regions with the aid of Fig. 2 below.

To obtain an approximate dispersion relation, and gain some physical insight into the nature of the interaction, we return to Eqs. (1) and (2). Still taking λ to be a constant,

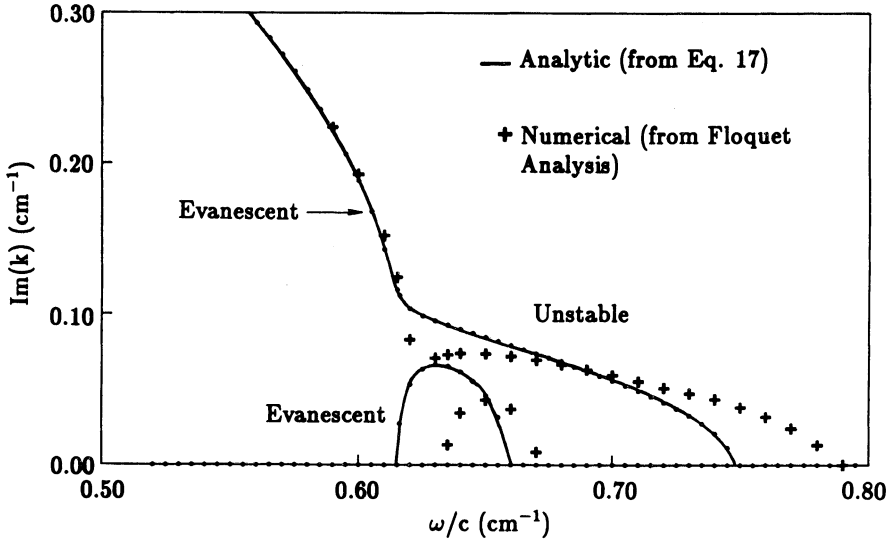

FIGURE 1: Spatial growth rate $Im(k)$ vs. ω/c (real) for the parameters of Table 1. Values obtained from the Floquet formulation (+) are compared to values obtained from the approximate dispersion relation, Eq. (17). The TE_{11} cutoff occurs at $\omega/c \approx 0.614$ cm^{-1}.

we formally take Fourier transforms in both t and z: $\partial/\partial t \longrightarrow -i\omega$; $\partial/\partial z \longrightarrow ik$. Equation (2) then gives

$$a_{\omega,k} = \frac{2\pi i k_\perp^2}{I_{1n} c} \frac{(\omega - k v_z)\, \lambda \eta_{\omega,k}}{\omega^2/c^2 - k^2 - k_\perp^2} \quad . \tag{7}$$

Let us expand

$$\Omega^2(z) = \sum_{\ell=-\infty}^{\infty} \Omega_\ell^2 e^{i\ell k_q z} \quad , \tag{8}$$

where $k_q \equiv 2\pi/L$ and $\Omega_{-\ell}^2 = \Omega_\ell^{2*}$ since $\Omega^2(z)$ is real. Then Eqs. (1) and (7) yield the following infinite set of coupled equations:

$$-(\omega - k v_z)^2 \eta_{\omega,k} + \sum_{\ell=-\infty}^{\infty} \Omega_\ell^2 \eta_{\omega,k+\ell k_q} = \frac{-\epsilon_n k_\perp^2 (\omega - k v_z)^2 \eta_{\omega,k}}{\omega^2/c^2 - k^2 - k_\perp^2} \tag{9}$$

where $\epsilon_n = 2\pi\nu/(\gamma I_{1n})$ is a dimensionless coupling constant and ν is Budker's parameter, $\nu = -e\lambda/mc^2$. The basic dispersion relation is obtained by setting the infinite determinant of coefficients in Eq. (9) to zero.

We consider first the elementary case $\Omega_0^2 > 0$, $\Omega_\ell^2 = 0$ for $\ell \neq 0$, that is, the case of either weak focusing or the smooth approximation to strong focusing. In this case there is no coupling among wave numbers and the dispersion relation becomes

$$\left[(\omega - k v_z)^2 - \Omega_0^2\right] \left[\omega^2 - \left(k^2 + k_\perp^2\right) c^2\right] = \epsilon_n k_\perp^2 c^2 (\omega - k v_z)^2 \tag{10}$$

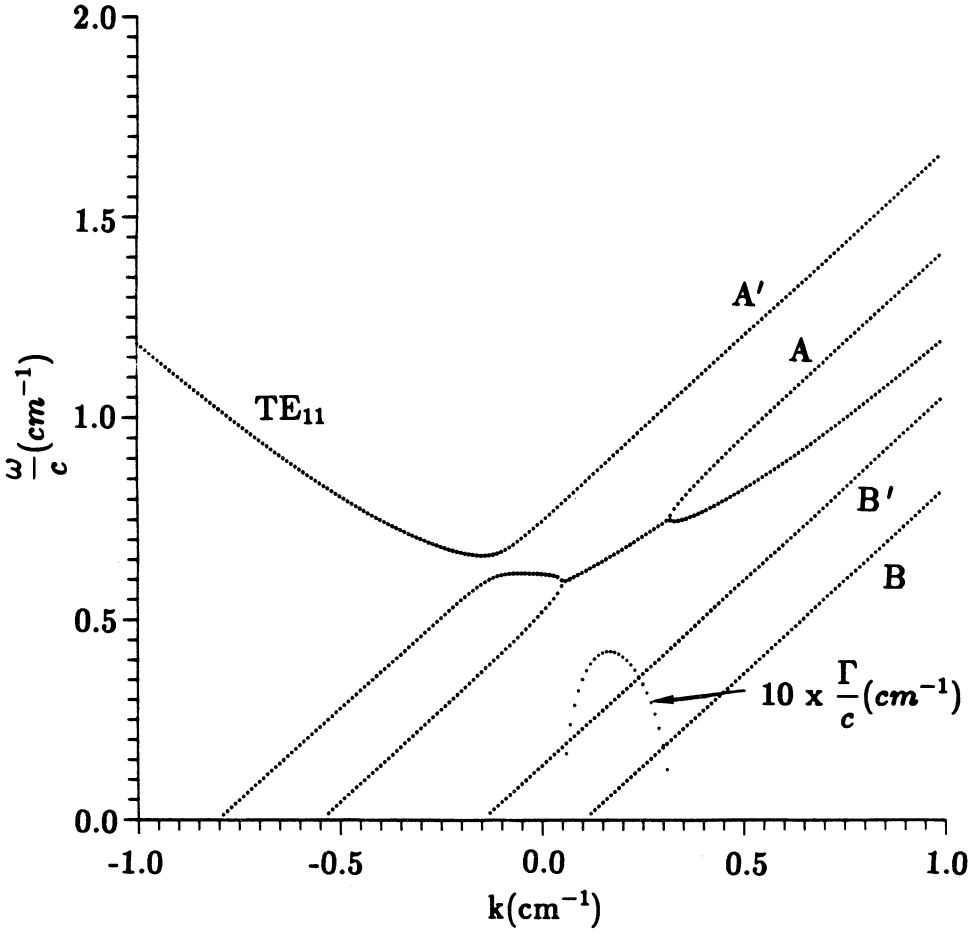

FIGURE 2: Solution to dispersion relation, Eq. (17), for parameters in Table 1 for real k. The intersection of the slow sideband mode, A, with the TE_{11} mode produces an unstable region with growth rates $\Gamma(k)$.

Depending upon the relative sizes of the betatron frequency Ω_0 and the waveguide cutoff frequency, $k_\perp c$, there may or may not be intersections between the beam modes

$$\omega - kv_z = \pm\Omega_0 \tag{11}$$

and the waveguide modes

$$\omega^2 = \left(k^2 + k_\perp^2\right) c^2 \quad , \tag{12}$$

as shown in Fig. 3. The condition for such intersections to exist is

$$\Omega_0^2 > k_\perp^2 c^2/\gamma^2 \quad , \tag{13}$$

but it is straightforward to show that these intersections are stable for small ϵ_n. The situation is different, however, when AG focusing is imposed.

Consider the case $\Omega_0^2 = 0$, which includes the simple FODO lattice. Without loss of generality, we may choose the origin in z so that $\Omega_1^2 = \Omega_{-1}^{2*}$ is purely imaginary. Let us now retain only the $\ell = \pm 1$ terms in Eq. (9), an approximation justified later for the lattice example solved numerically below. Equation (9) becomes

$$-(\omega - kv_z)^2 \eta_k + \frac{\alpha}{2i}\left(\eta_{k-k_q} - \eta_{k+k_q}\right) = \frac{-\epsilon_n k_\perp^2 (\omega - kv_z)^2 \eta_k}{\omega^2/c^2 - k^2 - k_\perp^2} \quad , \tag{14}$$

where $\alpha = -2i\Omega_1^2$ and we have dropped the subscript ω. The dispersion relation we seek is obtained by setting to zero the determinant of the infinite set of equations given by Eq. (14).

At this point, we consider the approximate dispersion diagram in Fig. 4. We see that although the beam mode $\omega = kv_z$ cannot intersect the TE_{1n} mode, the sidebands at $\omega = (k \pm k_q)v_z$ may do so. It is these intersections that give rise to the beam centroid instability. In Fig. 4 it is sufficient to consider only the upper half-plane ($Re(\omega) > 0$). The lower half-plane is symmetric with the upper under the replacements $k \rightarrow -k$, $\omega \rightarrow -\omega^*$.

Suppose that for a given k, we keep only the k and $k \pm k_q$ components in the Fourier expansion of η. Writing the equation for η_{k+k_q} ($k \longrightarrow k + k_q$ in Eq. (14)), and neglecting the right-hand side (since the denominator is not small near the intersections of the $\omega = (k + k_q)v_z$ sideband with the TE_{1n} mode), we find

$$\eta_{k+k_q} \approx \frac{\alpha/2i}{(\omega - kv_z - k_q v_z)^2}\eta_k \quad . \tag{15}$$

Similarly, we find

$$\eta_{k-k_q} \approx \frac{-\alpha/2i}{\left(\omega - kv_z + k_q v_z\right)^2}\eta_k \quad , \tag{16}$$

but the denominator of Eq. (16) is not small near the intersections in Fig. 4 and so we neglect η_{k-k_q} in comparison with η_{k+k_q}. Then, substitution of Eq. (15) in (14) gives the following approximate dispersion relation

$$(\omega - kv_z)^2 - \left(\frac{\alpha}{2}\right)^2 \frac{1}{\left(\omega - kv_z - k_q v_z\right)^2} - \frac{\epsilon_n k_\perp^2 (\omega - kv_z)^2}{\omega^2/c^2 - k^2 - k_\perp^2} = 0 \quad . \tag{17}$$

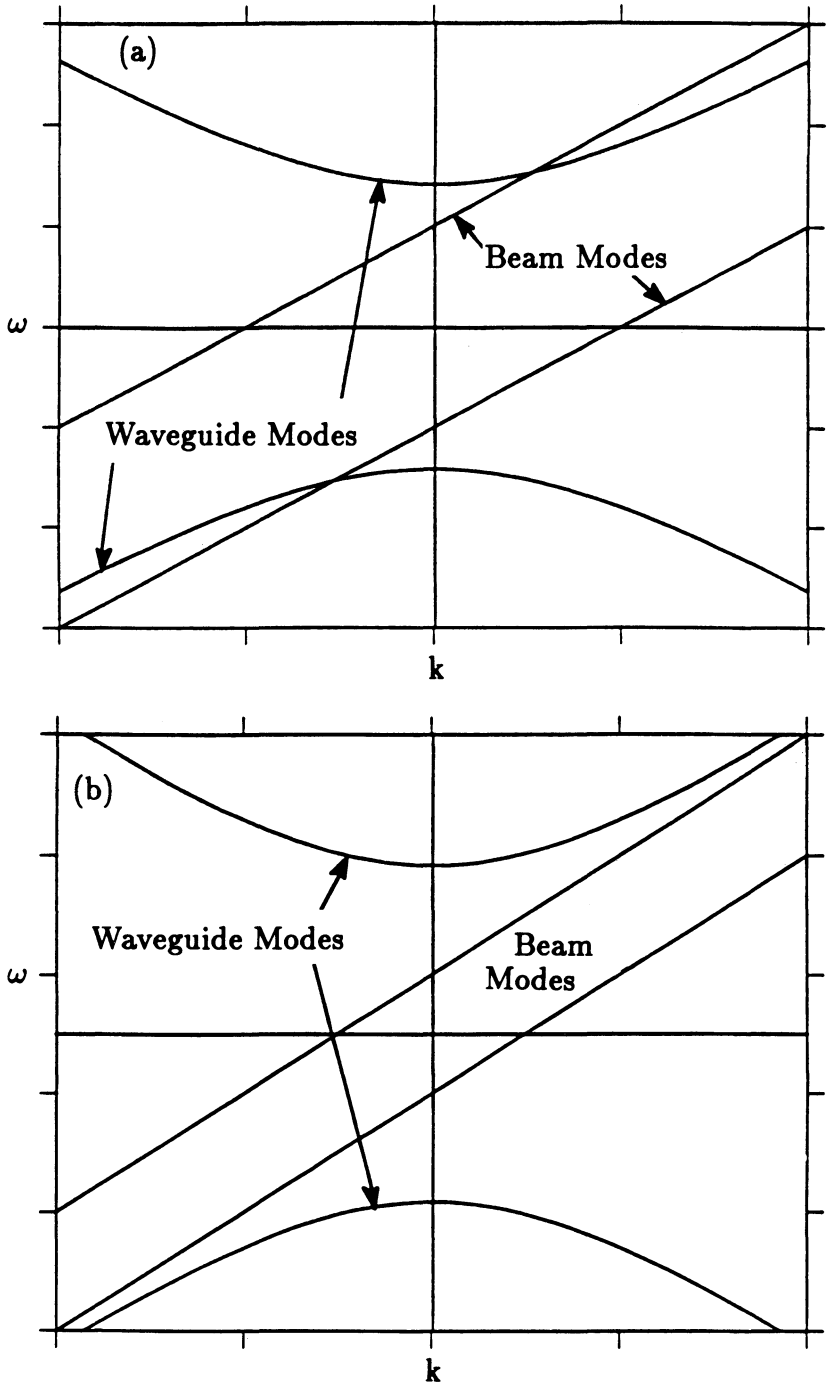

FIGURE 3: Dispersion ($\omega - k$) diagrams showing the possibilities of intersection (a) or non-intersection (b) of the beam modes and waveguide modes for the case of weak focusing.

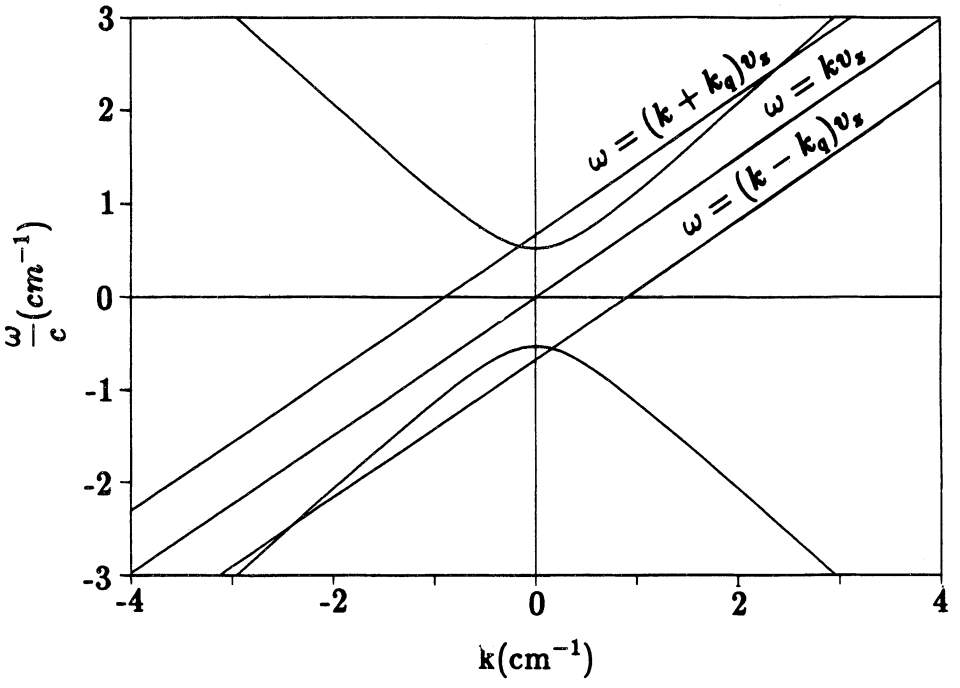

FIGURE 4: Dispersion diagram illustrating intersection of sidebands, $\omega = (k \pm k_q)v_z$, with TE_{1n} mode of drift tube. (Numbers correspond to $\gamma = 1.5$, $b = 3.4$ cm, $k_q = 0.9$ cm^{-1}, $n = 1$).

This sixth-order polynomial dispersion relation can be approximated with a cubic expression by expanding about the intersections of the beam and pipe modes, but simple analytic expressions for the instability growth rate are not readily obtainable. However, an approximate criterion for the existence of the instability can be given. In order for the lines $\omega = (k + k_q)v_z$ and $\omega = c\sqrt{k^2 + k_\perp^2}$ to cross — that is, in order for the instability to occur — it is necessary that

$$k_q \geq \frac{k_\perp c}{\gamma v_z} \quad . \tag{18}$$

The group velocity, v_g, of the instability is given approximately by the average of the group velocities of the uncoupled modes at the point of intersection, i.e.,

$$v_g \approx \frac{1}{2}\left(\frac{\partial \omega_b}{\partial k} + \frac{\partial \omega_{em}}{\partial k}\right) = \frac{1}{2}\frac{k\left(1 + v_z/c\right) + k_q}{k + k_q} \quad , \tag{19}$$

where $\omega_b = (k + k_q)v_z$ and $\omega_{em} = c\sqrt{k^2 + k_\perp^2}$. This result is empirical, but agrees well with numerical calculations (see Section 3).

In Fig. 2, we show the numerical solution to Eq. (17) for the parameters in Table 1, which are characteristic of those of an injector for an induction linac. The lowest fre-

TABLE 1: Parameters for Example in Figs. 1, 3, 5 and 6.

Beam Energy (γ)	2.5
Beam Current	1 kA ($\nu = 0.064$)
Circular Pipe Radius (b)	3 cm
Quadrupole Period (L)	9 cm
Quadrupole Gradient	520 gauss/cm

quency transverse-electric mode for a beam-pipe of circular cross-section is the TE_{11} mode, for which $\epsilon \approx 2.472\nu/\gamma$. Note that the pair of beam modes, $(\omega - kv_z)^2 \approx 0$ (A, A' in Fig. 2) and the pair of sidebands, $(\omega - kv_z - k_q v_z)^2 \approx 0$, ($B, B'$ in Fig. 2) are strongly split by the interaction. The peak growth rate $\Gamma_{\max}$, is approximately 1.25 e-folds/ns, and the corresponding group velocity is $0.595c$.

The quadrupole gradient required to focus this beam, assuming it is space-charge-dominated, is given approximately by[11]

$$\nabla B_0 \approx \frac{mc}{e}\frac{1}{r_b L}\left(\frac{96\nu}{\gamma}\right)^{1/2} , \tag{20}$$

where r_b is the beam radius. The value of 520 gauss/cm in Table 1 is consistent with $r_b \approx 0.57$ cm. Note that the dispersion relation, Eq. (17), does not depend on the beam radius.

3 NUMERICAL SIMULATION OF INSTABILITY

In the derivation of the dispersion relation, Eq. (17), several approximations were made. In particular, only the $\ell = \pm 1$ terms in Eq. (9) were retained, and only the wavenumbers k and $k + k_q$ were retained in the Fourier expansion of the beam centroid. To see the effect of relaxing these assumptions, we have carried out numerical simulations of the instability. The computer code written for this purpose advances a train of macroparticles representing the beam centroid and computes the axial variation of the electromagnetic fields on a one-dimensional grid. We use discretized forms of Eqs. (1) and (2), assuming, as in the analytic derivation, that the beam is close to the center of the pipe. Arbitrary externally applied magnetic fields can be specified. A more complete description of the simulation code is given in Appendix B.

For the FD lattice we have run a simulation using the parameters in Table 1. The simulation is carried out in the beam frame, using a transformation $z \rightarrow z - v_z t$, and the beam is perturbed by giving the first macroparticle a small transverse displacement. This results in a growing wavepacket which convects towards the tail of the beam. In Figs. 5a and 6a, we show the beam centroid and the electromagnetic field (actually $d(ea/mc^2)/dt$; see Appendix B). We find that the corresponding spatial Fourier spectra

in Figs. 5b and 6b are consistent with the simplifications used to obtain Eq. (17). It is apparent that the two strongest modes in the beam centroid motion (Fig. 5b) are at wavenumbers $k_0 + k_q = 0.91$ cm^{-1} and $k_0 \equiv 0.21$ cm^{-1}. These are the wavenumbers of the terms η_{k+k_q}, η_k, which were argued to be dominant in the vicinity of $k = k_0$ in deriving Eq. (17). The weaker modes at $k = 0.5$, 1.6 cm^{-1} can be identified with the terms η_{k-k_q} and η_{k+2k_q}, respectively. These and higher-harmonic terms were dropped in the derivation. In the field power spectrum in Fig. 6b, the dominant spatial mode is at $k_0 = 0.21$ cm^{-1}. The smaller peaks at 0.5 cm^{-1} $(k_0 - k_q)$, 0.92 cm^{-1} $(k_0 + k_q)$, 1.2 cm^{-1} $(k_0 - 2k_q)$, 1.6 cm^{-1} $(k_0 + 2k_q)$ have amplitudes two orders or more lower than the dominant peak. In the derivation, the only electromagnetic term retained was that with wavenumber $k = k_0$.

We obtain a growth rate from the numerical simulation by plotting the peak displacement of the wavepacket versus time, as shown in Fig. 7a. A fit to the exponential-growth part of the curve gives $\Gamma/c \approx 0.038$ cm^{-1}. This agrees well with the value of 0.04 cm^{-1} at $k = 0.21$ cm^{-1} from the dispersion relation Eq. (17) as plotted in Fig. 2. The peak growth rate in Fig. 2 is $\Gamma_{\max}/c = 0.042$ cm^{-1} at $k = 0.17$ cm^{-1}. From Fig. 5b we see that the wavepacket contains a relatively broad range of wavenumbers (the FWHM of the main peak is ≈ 0.04 cm^{-1}), so it is not too surprising that the growth rate of the wavepacket is less than the peak linear growth rate. The group velocity of the wavepacket is obtained by plotting the axial position of the peak displacement vs. time, as in Fig. 7b. Since the simulation is carried out in the beam frame, this peak moves back from the beam head with velocity $v_g - v_b$. A linear fit gives a laboratory-frame velocity of $v_g \approx 0.6c$. This again agrees well with the value of $0.606c$ obtained from Eq. (19) for $k = 0.21$ cm^{-1}. The numerical solution in Fig. 2 gives $v_g = 0.595c$ at $k = 0.17$ cm^{-1}, and $v_g = 0.62c$ at $k = 0.21$ cm^{-1}.

4 ADDITIONAL EXAMPLES

In the previous sections, we looked at an example of instability growth in a transport system for a low-energy, high-current electron beam. There is some evidence[12] that this instability has in fact been observed in a transport system in which a continuous helical quadrupole,[5,8] rather than a set of discrete quadrupoles, was used. In this section, we briefly look at the possibility of the instability occurring in two other beam transport systems of current interest, namely, a high-energy storage ring and a heavy-ion quadrupole channel.

4.1 High-Energy Electron Storage Ring

We consider the parameters in Table 2, which are derived from those for the Advanced Light Source (ALS) at LBL. Since the magnet lattice and beam pipe in a machine such as the ALS are complex structures, however, we consider a much simplified configuration. We assume that the horizontal tune, ν_x, is produced by a simple FODO lattice with phase-shift $\pi/2$. This requires a quadrupole field strength $\nabla B_0 = 477$ gauss/cm, and quadrupole period of $4L = 344.4$ cm. We also assume that the beam is drifting in a cylindrical pipe

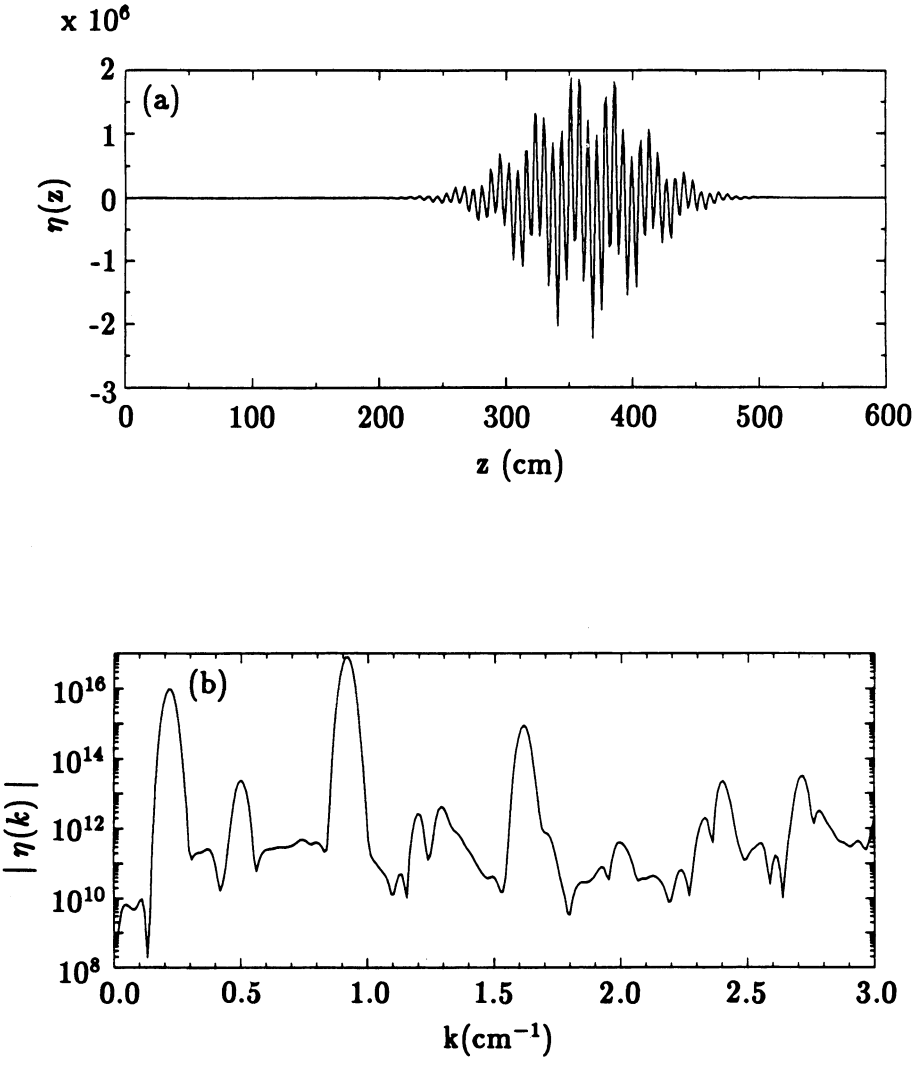

FIGURE 5: Beam displacement vs. z at one instant in time is shown in (a), and its spatial Fourier transform is shown in (b). Since the equations of motion are linear in η, the scale of η is arbitrary.

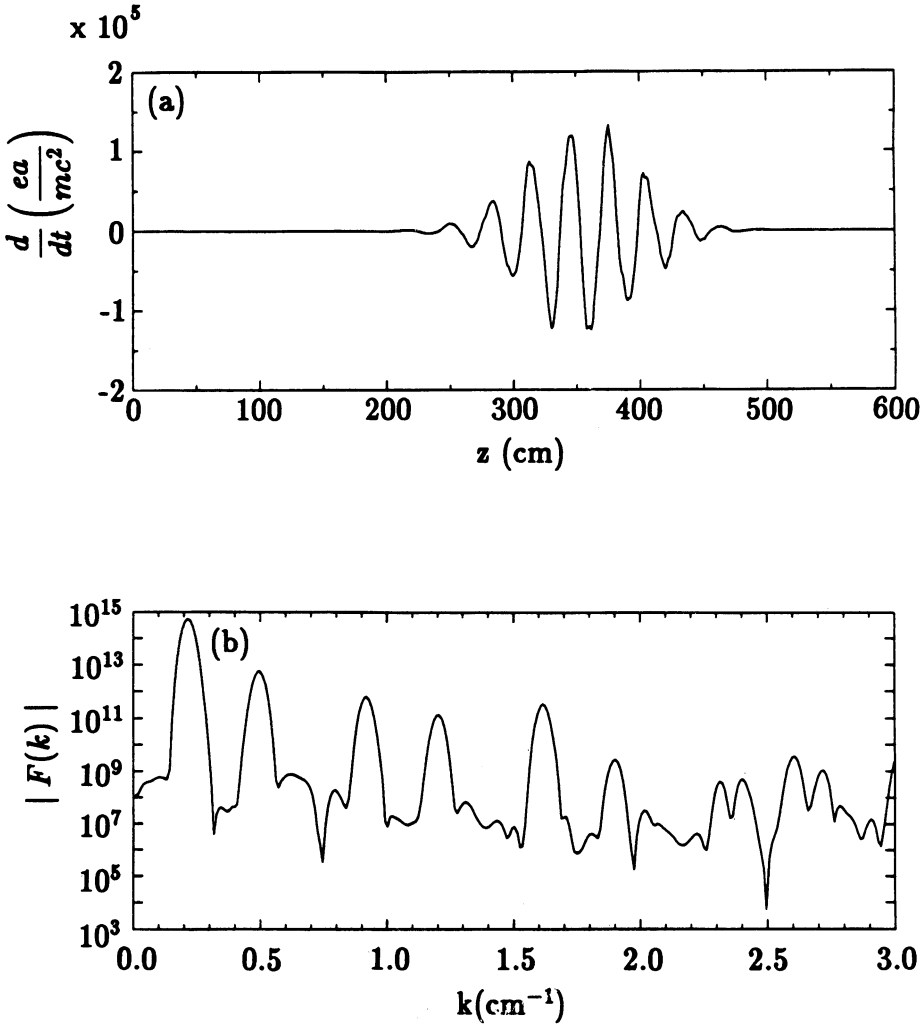

FIGURE 6: Electromagnetic field amplitude vs. z at same instant as Fig.5 is shown in (a). The spatial Fourier transform is in (b).

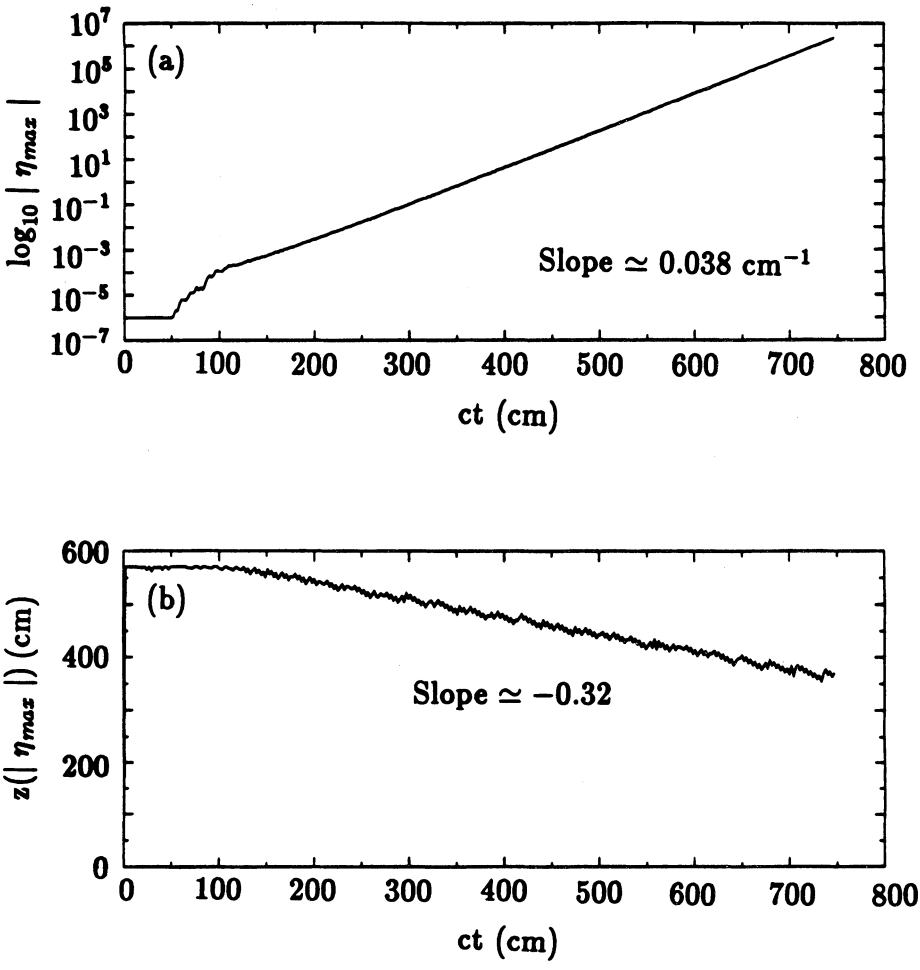

FIGURE 7: Numerical simulation results showing (a) exponential growth of peak of wavepacket and (b) position of peak vs. time. The wavepacket moves backwards in beam frame.

TABLE 2: Sample high-energy storage-ring parameters

Beam Energy	1.5 GeV
Pipe Radius	2.5 cm
Peak Current	100 A
Horizontal Tune	14.28
Machine Circumference	196.8 m

of constant radius. Solving Eq. (17) numerically, we find that an instability occurs for wavenumbers in the range 18.1–18.2 cm^{-1} (wavelength ≈ 3.45 mm), with an e-folding time of 1.6 μs. From Eq. (19), the group velocity is approximately equal to c.

Finite-Q effects, which have been neglected heretofore, are likely to have a significant stabilizing influence on this mode. We can include finite-Q effects in our model in an approximate way by replacing the resonant denominator $(\omega^2/c^2 - k^2 - k_\perp^2)^{-1}$ by $(\omega^2/c^2 + (i\omega/Q)\omega_0 - k^2 - k_\perp^2)^{-1}$, where $\omega_0(k) = c\sqrt{k^2 + k_\perp^2}$. We find that finite-$Q$ effects become important for $Q \approx \omega_0/2\Gamma$, where Γ is the growth rate obtained from the dispersion relation when $Q = \infty$. Applying this criterion to the growth rate just obtained, we find that for $Q \lesssim 4.5 \times 10^5$, the mode is stabilized. The Q value is related to the wall conductivity by $Q \approx \sqrt{2\pi\sigma\omega}\, b/c$, where σ is the conductivity. For stainless steel, for example, $\sigma \approx 1.25 \times 10^{16}$ s^{-1}, and we obtain $Q \approx 1.7 \times 10^4$ for $b = 2.5$ cm, $\omega/c \approx 18$ cm^{-1}. A simple treatment of Landau damping leads to the conclusion that an energy spread of $\Delta\gamma/\gamma \gtrsim \nu_x^2\Gamma/kc \approx 2.3 \times 10^{-4}$ should also stabilize the mode.

4.2 Heavy-Ion Quadrupole Channel

We consider the heavy-ion quadrupole channel example discussed by Reiser in Sec. 4.3 of Reference 11, Example 1(c). The relevant parameters are given in Table 3.

We see that for the fundamental spatial mode of the quadrupole field (wavenumber k_q), the instability condition, Eq. (18), is not satisfied. For the other examples in Reference 11, the condition is even further from being satisfied. However, higher spatial harmonics of the quadrupole field produce beam sideband modes that may give rise to instability. For the nth harmonic, the instability condition becomes $nk_q > k_\perp c/\gamma v_z$. For the case in Table 3, the 9th harmonic (wavenumber $9k_q$) is the lowest one that satisfies this condition. To compute a growth rate, we must scale the parameters α and ϵ_n in Eq. (14) as follows:

$$\begin{aligned} \alpha &\propto Zm/M \\ \epsilon_n &\propto Z^2 m/M \quad , \end{aligned}$$

where Z, M are the ion charge state and mass, respectively. The appropriate coefficient in the Fourier expansion of the quadrupole field is used in computing α. Due to the high ion mass, we find that the peak growth rate is only 0.14 μs^{-1}, occurring at a wavelength

TABLE 3: Sample heavy ion (U-238) channel parameters

Beam Charge State (Z)	10
Beam Current/Z (kA)	2
Beam Energy (GeV)	40
Pipe Radius (cm)	11.8
$k_\perp c/\gamma v_z$ (m^{-1})	25
Quadrupole Period (m)	2
k_q (m^{-1})	3.1
Quadrupole Gradient (gauss/cm)	2.97×10^3

and frequency of 5.1 m and 0.74 GHz. Following the discussion of finite Q effects in Section 4.1, one would expect significant stabilization of the mode for $Q \lesssim 1.7 \times 10^4$.

We note that, for the example in Table 1, where the fundamental spatial mode of the quadrupole field produces an instability, the higher spatial harmonics give rise to additional instabilities. However, the growth rates computed for these other modes are significantly less than that for the fundamental.

5 CONCLUSIONS

We predict a parametric instability in AG focusing systems due to an interaction between transverse sideband modes of the beam centroid and electromagnetic modes of the drift tube. Analytic expressions for the dispersion relation and instability criterion are obtained. The analytic predictions are in agreement with numerical simulation results from a rigid-disk code. We believe that this instability is likely to arise primarily in high-current, low-energy electron-beam transport systems. Growth rates obtained for sample high-energy electron storage ring and heavy-ion transport systems are small, and likely to be substantially further reduced by finite-Q effects. In regimes where the instability may be of concern, possible damping mechanisms include variation of the quadrupole period, variation of the drift-tube radius, and beam energy spread, in addition to finite-Q effects.

6 ACKNOWLEDGMENTS

This work was supported by the Defense Advanced Research Projects Agency, under ARPA Order No. 7792, and monitored by the Naval Surface Warfare Center.

REFERENCES

1. E. D. Courant and H. S. Snyder, Ann. Phys. **3**, 1 (1958).
2. S. Humphries, Jr., *Principles of Charged Particle Acceleration* (J. Wiley, New York, 1986), Chap. 8.
3. I. Hofmann, L. J. Laslett, L. Smith, and I. Haber, Part. Accel. **13**, 145 (1983).
4. J. Struckmeier, J. Klabunde, and M. Reiser, Part. Accel **15**, 47 (1984).
5. T. P. Hughes and B. B. Godfrey, Phys. Fluids **29**, 1698 (1986).
6. C.-M. Tang, P. Sprangle, J. Krall, P. Seraphim, and F. Mako, Part. Accel. **35**, 101 (1991).
7. J. Krall, C.-M. Tang, G. Joyce, and P. Sprangle, Phys. Fluids **B3**, 204 (1991).
8. C. W. Roberson, A. Mondelli, and D. Chernin, Part. Accel. **17**, 79 (1985).
9. W. H. Louisell, *Coupled Mode and Parametric Electronics* (J. Wiley, New York, 1960), Chap. 8.
10. R. J. Briggs, *Electron-Stream Interaction with Plasmas* (MIT Press, 1964).
11. M. Reiser, Part. Accel. **8**, 167 (1978).
12. M. Tiefenback and S. Putnam, private communication.
13. *Handbook of Mathematical Functions*, M. Abramovitz and I. A. Stegun, eds., (National Bureau of Standards, 1972), Sec. 11.4.
14. W. F. Ames, *Numerical Methods for Partial Differential Equations*, p. 200 (Academic Press, 1977).
15. B. B. Godfrey, J. Comp. Phys. **15**, 504 (1974).

APPENDIX A. FIELD EQUATION

A TE_{mn} mode in a smooth cylindrical pipe of radius b is described by the vector potential

$$A_{mn;r} = \frac{m}{k'_{mn} r} J_m\left(k'_{mn} r\right) e^{im\theta} \tag{21}$$

$$A_{mn;\theta} = iJ'_m\left(k'_{mn} r\right) e^{im\theta} \quad , \tag{22}$$

where $k'_{mn} = j'_{mn}/b$, $J'_m(j'_{mn}) \equiv 0$, and the r and θ subscripts denote radial and azimuthal components. In general, the total vector potential (in the Lorentz gauge) satisfies

$$\left(\nabla^2 - \frac{1}{c^2}\frac{\partial^2}{\partial t^2}\right)\vec{A} = -\frac{4\pi}{c}\vec{J} \quad , \tag{23}$$

where $\vec{J}$ is the total current. If we expand $\vec{A}$ in terms of TE modes,

$$\vec{A} = \sum_{m,n} a_{mn}(z,t)\vec{A}_{mn} \quad , \tag{24}$$

we find that

$$\left[\frac{\partial^2}{\partial z^2} - \frac{1}{c^2}\frac{\partial^2}{\partial t^2} - k'^2_{mn}\right] a_{mn}(z,t) = -\frac{4\pi}{c}\frac{\int r dr d\theta \vec{A}^*_{mn} \cdot \vec{J}}{\int r dr d\theta \mid \vec{A}_{mn} \mid^2} \quad , \tag{25}$$

where an asterisk denotes the complex conjugate. Confining our attention now to $m = 1$, and assuming that the beam is close to the axis, we find

$$\int r dr d\theta \vec{A}^*_{1n} \cdot \vec{J} \approx \frac{\lambda}{2}\dot{\eta} \quad , \tag{26}$$

where λ is the beam charge per unit length and η is the displacement of the centroid from the axis. The normalization integral in the denominator of Eq. (25) can be calculated from standard Bessel function identities[13]; its value is

$$\int r dr d\theta \mid \vec{A}_{mn} \mid^2 = \pi \left(j'^2_{mn} - m^2\right) J_m^2 \left(j'_{mn}\right) / k'^2_{mn} \quad . \tag{27}$$

Using Eqs. (26) and (27) in (25) yields Eq. (2) in the text.

APPENDIX B. NUMERICAL SIMULATION CODE

A computer code, E3WAVE, was written to simulate the linear behavior of the parametric instability. As in the analytic model in Section 2, the beam is represented by a string of disks moving at constant velocity v_z. We discretize Eq. (1) as

$$\frac{\eta^{N+1} - 2\eta^N + \eta^{N-1}}{\Delta t^2} = -\Omega^2(z)\eta^N + \frac{e}{\gamma mc}\dot{a}^N \quad , \tag{28}$$

where Δt is the timestep and N denotes the Nth timestep.

Taking the convective derivative of the field equation, Eq. (2), we obtain

$$\left(\frac{\partial}{\partial z^2} - \frac{1}{c^2}\frac{\partial}{\partial t^2} - k_\perp^2\right)\frac{e\dot{a}}{mc^2} = -\frac{2\pi\nu k_\perp^2}{I_{1n}c}\ddot{\eta} \quad . \tag{29}$$

To solve this equation in the laboratory (z, t) frame, we use an implicit discretization of the left-hand side described by Ames,[14] treating $e\dot{a}/mc^2$ as the dependent variable. A relaxation parameter is adjusted to damp out a numerical Cherenkov instability.[15] Equations (28) and (29) are advanced in leapfrog fashion. For simplicity, the beam disks are advanced one mesh spacing Δz per timestep. The timestep and mesh spacing are thus related by $\Delta z = v_z \Delta t$. In choosing Δz, the wavelengths associated with the quadrupole field, the transverse particle motion, and the electromagnetic field must be resolved.

To do simulations in beam-frame, as was done for Fig. 7, Eq. (29) is transformed to coordinates $s = z - v_z t$, $\tau = t$. The left-hand-side operator becomes

$$\frac{1}{\gamma^2}\frac{\partial^2}{\partial s^2} - \frac{1}{c^2}\frac{\partial^2}{\partial \tau^2} + 2v_z\frac{\partial^2}{\partial \tau \partial s} - k_\perp^2 \quad .$$

A simple implicit discretization of $\partial/\partial\tau$, $\partial^2/\partial\tau^2$ is used. The beam disks do not move axially in the s, τ frame, and the timestep and mesh spacing can be chosen independently.